nature structural & molecular biology

Substrate-modulated ADP/ATP-transporter dynamics revealed by NMR relaxation dispersion

Sven Brüschweiler[1,4], Qin Yang[1,4], Changqing Run[2,3] & James J Chou[1–3]

The ADP/ATP carrier (AAC) transports ADP and ATP across the inner mitochondrial membrane. Unlike most transporters, which have two-fold direct or inverted quasisymmetry, AAC has apparent three-fold rotational symmetry. Further, its transport rate is relatively fast for transporters that carry large solutes. Here, we study the yeast AAC carrier 3 by obtaining comprehensive NMR relaxation dispersion measurements, which provide residue-specific information on the protein's conformational exchange. Our data indicate that AAC is predominantly in the cytosol-facing open state and converts to a sparsely populated state in an asymmetric manner despite its three-fold structural symmetry. Binding of the substrate ADP substantially increases the rate of conformational exchange, whereas the inhibitor CATR slows the exchange. These results suggest that although the transporter catalyzes the translocation of substrate the substrate also facilitates interconversion between alternating states, and this interconversion may be relevant to the transport function.

A key aspect of the transport mechanism of solute carriers is dynamic coupling between solute binding and a protein-conformational switch that facilitates solute translocation across the membrane[1,2]. With rapidly growing availability of crystal structures capturing various states of transporters and advances in molecular dynamics (MD) simulation techniques, addressing transporter conformational dynamics by computational means is becoming increasingly feasible[3–5]. However, experimental observation of transporter dynamics is still rare, and it has relied mostly on spectroscopic methods such as fluorescence resonance energy transfer (FRET). The high sensitivity of FRET affords measurement at the single-molecule level and has been used to provide insights into the dynamic properties of LacY, LeuT and Glt_{Ph}[6–10].

The use of NMR to investigate membrane-protein structures and dynamics is an emerging area of research[11–15]. NMR has much lower sensitivity than FRET, but it has the advantage of providing residue-specific information on conformational exchange. Because NMR experiments are sensitive to the timescale and magnitude of chemical exchange, they can be tailored to probe various dynamic processes of solute carriers. For systems that are slow on the NMR timescale, ZZ exchange[16,17] and chemical exchange saturation transfer[18] are sensitive methods for measuring protein conformational dynamics. For exchange processes on the microsecond-to-millisecond time scale, R_2 relaxation dispersion is the suitable probe[19,20], and it has been used successfully to detect sparsely populated states (known alternatively as 'invisible states')[21,22]. Thus far, the only comprehensive NMR measurement of conformational exchange of a membrane transporter has been on the multidrug-resistance transporter EmrE bound to the substrate tetraphenylphosphonium (ref. 13). In that study, ZZ-exchange measurements showed that EmrE undergoes conformational exchange with a rate constant of 4.8 s^{-1} between an inward- and an outward-facing state, and this conformational change is responsible for substrate transport through the membrane.

We sought to investigate the conformational dynamics of the mitochondrial AAC, an essential protein in eukaryotes that exchanges ADP and ATP across the inner mitochondrial membrane[23,24]. The AAC is a much faster transporter than EmrE; high-time-resolution measurements showed that the transport rates for ADP and ATP are 400 s^{-1} and 160 s^{-1}, respectively[25]. At this rate, ZZ exchange is not applicable, and NMR measurement of conformational exchange would require less sensitive methods for measuring R_2 relaxation dispersion. The AAC belongs to the mitochondrial carrier family (MCF) of transporters, which catalyzes the trafficking of metabolites and ions into and out of the matrix[23,26]. It is also the only MCF member for which high-resolution structures have been determined[27,28]. The crystal structures of AAC bound to the inhibitor carboxyatractyloside (CATR) resemble an open-top barrel formed by three structurally similar domains in parallel orientation (**Fig. 1a**,**b**). Each domain consists of two transmembrane (TM) helices separated by an amphipathic (AP) helix. It has been proposed that ADP/ATP transport involves interconversion between a cytosol-facing open state (c state) and a matrix-facing open state (m state)[24]. The crystal structure of AAC is open to the cytosol side and thus represents the c state. The m-state structure is still unknown.

Several open questions are associated with AAC and MCF members in general, particularly relating to their unusual structural symmetry

[1]Department of Biological Chemistry and Molecular Pharmacology, Harvard Medical School, Boston, Massachusetts, USA. [2]National Center for Protein Science, Shanghai Institute of Biochemistry and Cell Biology, Chinese Academy of Sciences, Shanghai, China. [3]State Key Laboratory of Molecular Biology, Shanghai Institute of Biochemistry and Cell Biology, Chinese Academy of Sciences, Shanghai, China. [4]These authors contributed equally to this work. Correspondence should be addressed to J.J.C. (james_chou@hms.harvard.edu).

Received 1 February; accepted 16 June; published online 13 July 2015; doi:10.1038/nsmb.3059

in comparison to that of most solute carriers. First, the AAC has a three-fold longitudinal quasisymmetry (with the symmetry axis perpendicular to the membrane) instead of the more common two-fold symmetry. It is unclear whether the AAC undergoes the 'V–to–inverted V' type of conformational switching, which has been proposed as a possible transport mechanism[24] and has been determined to be the transport mechanism for LacY[10] and EmrE[13]. Here, we performed comprehensive measurements of R_2 relaxation dispersion of the yeast AAC to address the intrinsic and the substrate- and inhibitor-modulated conformational exchange of this architecturally unorthodox solute transporter.

RESULTS

A functionally relevant NMR sample of AAC

We first produced an NMR-amenable and functionally relevant AAC sample. We expressed the yeast AAC carrier 3 (yAAC3) in *Escherichia coli* cells and purified the carrier by nickel–nitrilotriacetic acid affinity, ion exchange, ATP affinity and size-exclusion chromatography (Online Methods). We reconstituted the purified yAAC3 in dodecylphosphocholine (DPC) micelles at pH 6 for NMR measurements. Because AAC has a highly specific inhibitor, CATR, we used CATR binding to examine proper folding of yAAC3 in the NMR sample. Isothermal titration calorimetry (ITC) showed that CATR binds DPC-reconstituted yAAC3 with a K_d of ~15 μM (**Fig. 1c** and **Supplementary Fig. 1a**). Previously, a binding study with a more native inhibitor showed that atractyloside, a CATR derivative, binds yeast mitochondrial AAC carrier 2 (yAAC2) with a K_d of 192 μM (ref. 29). Another earlier study of ATP-transport inhibition showed that CATR binds to AAC about ten times more strongly than atractyloside[30,31]. The combined results indirectly suggest that the K_d of CATR binding to yAAC3 is ~20 μM under native conditions, a result consistent with our observed CATR binding in the NMR sample.

The sample yielded a good-quality NMR spectrum (**Fig. 1d**) that is characteristic of α-helical proteins. Chemical-shift changes of an 0.8-mM yAAC3 sample titrated with CATR indicated binding saturation at around 4 mM CATR (total inhibitor concentration). Simulated binding curves for various K_d values at fixed protein concentration (0.8 mM) indicated that the K_d from NMR titration is ~150 μM (**Supplementary Fig. 1b**,**c**). The increased K_d measured by NMR compared to ITC for CATR and ADP is most probably due to the increased detergent concentration necessary for NMR experiments. In NMR titration measurements, most of the residues expected to be involved in CATR binding showed a CATR concentration–dependent chemical-shift perturbation, including residues Lys27, Ile84, Arg85 and Thr86 (**Fig. 1e**). These residues interact with CATR according to the crystal structure of the yeast AAC–CATR complex determined recently[28]. We further showed by NMR titration that ADP addition leads to concentration-dependent chemical-shift perturbation for several cavity residues, including Arg141, which is believed to directly interact with ADP. Analysis of the titration data suggested a K_d of ~500 μM for ADP binding (**Supplementary Fig. 1d**,**e**). We further showed ADP binding with ITC (**Supplementary Fig. 1f**). The current and previous results together indicated that the yAAC3 reconstituted in DPC was suitable for both NMR and functional measurements.

Measurement of R_2 relaxation dispersion

Having obtained a functionally relevant NMR sample of yAAC3, we conducted relaxation dispersion measurements for the transporter in three different states: in the free form, in the presence of the substrate ADP and in the presence of the inhibitor CATR. The presence of a second less populated state in equilibrium with the major state of a protein leads to line broadening of the major-state NMR peaks, and this effect can be modulated by application of a train of 180° radio frequency (RF) pulses in the CPMG pulse sequence[19,20]. The shape of the resulting relaxation

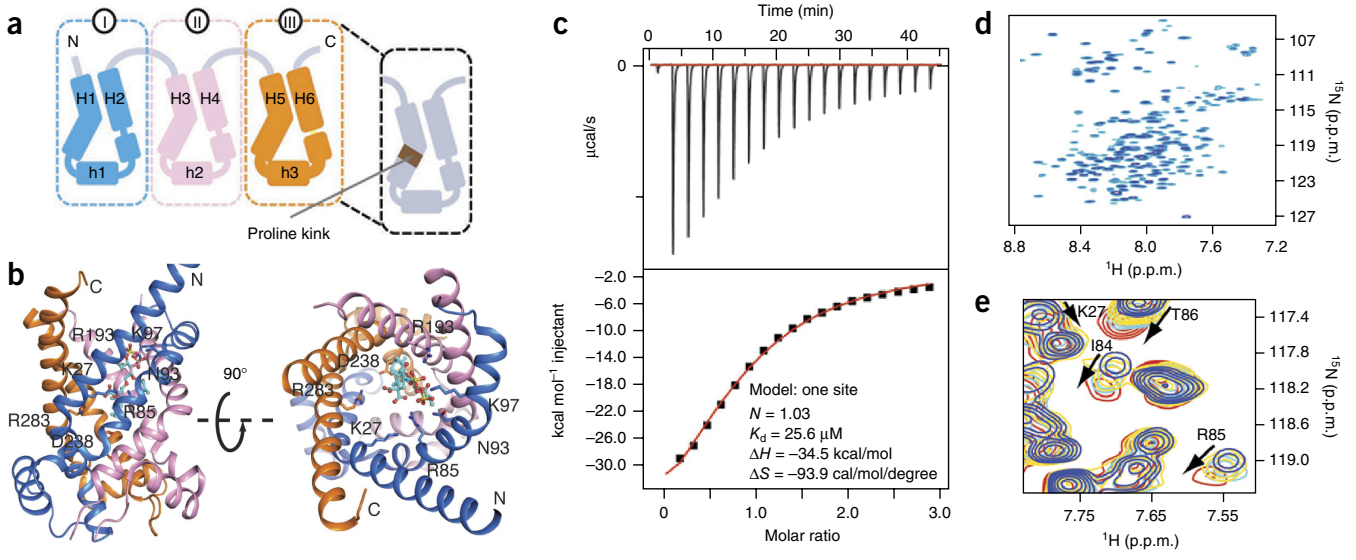

Figure 1 AAC architecture and its functional reconstitution in DPC. (**a**) Schematic of the tripartite topology of AAC. AAC is composed of three domains with homologous sequence and structure. Each domain contains two long TM helices and an amphipathic helix on the mitochondrial matrix side. Conserved prolines located approximately at the middle of the odd-numbered TM helices cause large kinks in these helices. (**b**) Ribbon representation of the crystal structure of the yAAC3–CATR complex (PDB 4C9Q[28]). Domains I–III are colored in blue, purple and orange, respectively, as in **a**. The CATR molecule is shown as cyan sticks. Labeled residues are those showing close contact with CATR. (**c**) ITC analysis of yAAC3 binding to CATR. The top and bottom graphs show the raw data and normalized integration data, respectively. Data fitting yields K_d = 14.9 ± 9.6 μM s.d. (n = 3 repeat experiments with K_d values of 25.6, 11.0 and 8.1 μM; data shown are values obtained from fitting the ITC curve in **c**). N, stoichiometry. (**d**) ^{15}N TROSY-HSQC spectrum of ^{15}N-^{13}C- and ^{2}H-labeled yAAC3 reconstituted in 120 mM DPC micelles at pH 6.0, recorded at 30 °C and ^{1}H frequency of 600 MHz. (**e**) A region of the ^{15}N TROSY-HSQC showing serial perturbation of several residues of yAAC3 (0.8 mM) involved in CATR binding, according to the crystal structure. The spectra were recorded at total CATR concentrations of 0 mM (blue), 1 mM (yellow), 2 mM (cyan) and 4 mM (red).

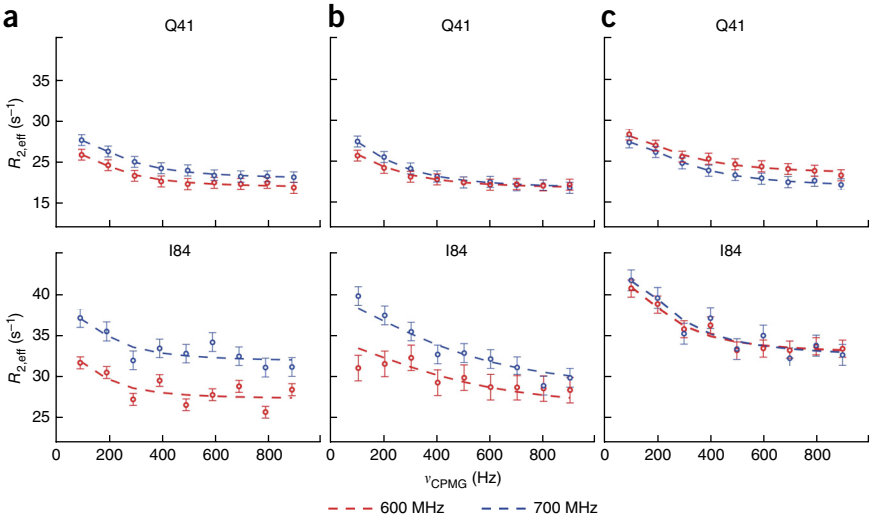

Figure 2 Conformational exchange detected by NMR relaxation dispersion. Examples of ^{15}N relaxation dispersion profiles for Gln41 and Ile84, measured at ^{1}H frequencies of 600 MHz (red circles) and 700 MHz (blue circles). ν_{CPMG}, CPMG-based RF field strengths; eff, effective. Error bars, s.d. ($n = 4$ repeat experiments). (**a**) Relaxation dispersion of yAAC3 in the absence of ligands. (**b**) Relaxation dispersion of yAAC3 in the presence of 10 mM ADP. (**c**) Relaxation dispersion of yAAC3 in the presence of 3 mM CATR.

dispersion curve depends on the population of the two states (p_i), the chemical-shift difference ($\Delta\omega$) and the rate of state interconversion (k_{ex})[19,20]. Because the backbone (^{1}H, ^{15}N) resonances of yAAC3 in a 2D ^{1}H-^{15}N correlation spectrum were very overlapped, we measured relaxation dispersion in the 3D mode by introducing the TROSY ^{15}N-CPMG element[32] into the 3D TROSY-HNCO pulse sequence (**Supplementary Fig. 2**). For peaks with lower signal-to-noise (SN) ratio, we used the more sensitive 2D TROSY-HSQC–based experiment. The combined data from 3D and 2D ^{15}N-CPMG experiments recorded at magnetic field strengths of 600 and 700 MHz allowed us to derive the microsecond-millisecond motion of ~95% of the assigned residues of free and ADP-bound yAAC3. For the CATR-bound state, a smaller number of residues could be analyzed, owing to decreased SN ratios.

AAC shows exchange between the c state and an excited state

We detected nonflat relaxation dispersion profiles for residues in the TM helices (H1–H3, H5 and H6) and the AP helices (h1 and h2) (examples in **Fig. 2a**). Fitting these curves individually to a numerical solution of the Bloch equation[33] yielded similar values of rates and populations for free yAAC3. For the ADP- and CATR-bound forms of yAAC3, however, the rates were different between the TM and AP helices. Therefore, when performing global fitting of dispersion data to a two-state exchange model[34,35] (Online Methods), we treated TM and AP regions separately for the three sample conditions, to obtain a consistent fit for all three states. For free yAAC3, the global fit yielded $k_{ex} \approx 870 \pm 200\ s^{-1}$ for TM and $940 \pm 170\ s^{-1}$ for AP regions (**Table 1** and **Supplementary Table 1**). The fit also yielded relative populations of $98.0 \pm 0.4\%$ and $2.0 \pm 0.4\%$ for the two states at equilibrium, with maximum $\Delta\omega$ as large as 5.7 p.p.m. in ^{15}N. To further validate the relaxation dispersion parameter obtained from two fields, we performed additional 2D relaxation dispersion experiments at 800 MHz for free AAC and AAC in the presence of ADP (**Supplementary Fig. 3**). Fitting data from all three fields to a two-state exchange model yielded very similar exchange parameters (**Supplementary Table 2**). Because the NMR spectrum of free yAAC3 is very similar to that of CATR-bound yAAC3, the major population should be in the c state (or the ground state). The c state transiently converts to a sparsely populated excited state. Although there is no direct information on the conformation of the excited state, it is expected to be structurally distinct from the c state because of the large $\Delta\omega$ values.

Modulation of AAC dynamics by inhibitor and substrate

The addition of 3 mM CATR decreased the exchange rate for the TM region by more than five-fold ($k_{ex} = 150 \pm 110\ s^{-1}$) (**Fig. 2c** and **Table 1**), as expected from binding of the inhibitor to the cavity of the transporter. But remarkably, the presence of 10 mM ADP, which is also believed to bind the cavity, increased the exchange rate of the TM region by more than two-fold ($k_{ex} = 1{,}800 \pm 350\ s^{-1}$) (**Fig. 2b** and **Table 1**). This observation indicates that ADP facilitates the conversion between the c state and the excited state. For binding of both inhibitor and substrate, the exchange rate of the AP helices was not substantially affected, thus suggesting that the intrinsic motion of the AP helices is subject to a different mode than the TM region. This is consistent with the AAC structure, in which the loops connecting the AP helices to the TM helices are mostly flexible[27,28]. In both cases of binding of CATR and ADP, the relative populations of the two states also did not appear to be affected, although the uncertainties were substantially larger than those of fitting results for free yAAC3 (**Table 1** and **Supplementary Table 1**).

AAC conformational exchange is asymmetric

Despite the three-fold quasisymmetry of the AAC structure, the residues that show substantial exchange were asymmetrically distributed (**Fig. 3a**). The large exchanges were concentrated in domain I, and the kink region of H1 showed the strongest chemical exchange. For example, $\Delta\omega$ of Ala26 and Ser31 were 5.7 ± 0.9 and 5.5 ± 1.4 p.p.m., respectively (**Fig. 3b**). Moreover, the binding of ADP or CATR did not substantially alter the pattern of affected residues (**Supplementary Fig. 4**). The large chemical-shift differences between the ground and excited states are indicative of a major conformational rearrangement in that region. The peaks corresponding to the H3 kink region were too broad and weak to be analyzed; however, the strong line broadening is probably also due to microsecond-millisecond exchange. Several residues on the matrix side of H1, H3 and H5 showed exchange as well, including residues that belong to the AAC signature sequence, for example, Gln41, Ala146 and Met246. These residues are parts of helical segments that pack with each other to close the matrix side of the cavity. Chemical exchange in this region is probably associated with opening of the cavity to the matrix side.

Table 1 Kinetic and thermodynamic parameters of yAAC3 derived from relaxation dispersion measurements

State	Protein region	k_{ex} (s^{-1})	p_e (%)[a]
Free yAAC3	TM helices	870 ± 200	2.0 ± 0.4
	AP helices	940 ± 170	2.0 ± 0.4
yAAC3–ADP	TM helices	1,800 ± 350	2.0 ± 0.6
	AP helices	770 ± 450	2.0 ± 0.6
yAAC3–CATR	TM helices	150 ± 110	2.0 ± 1.5
	AP helices	1,040 ± 300	2.0 ± 1.0

[a]The symbol p_e denotes the population of the excited state. Errors are s.d. ($n = 4$ repeat experiments).

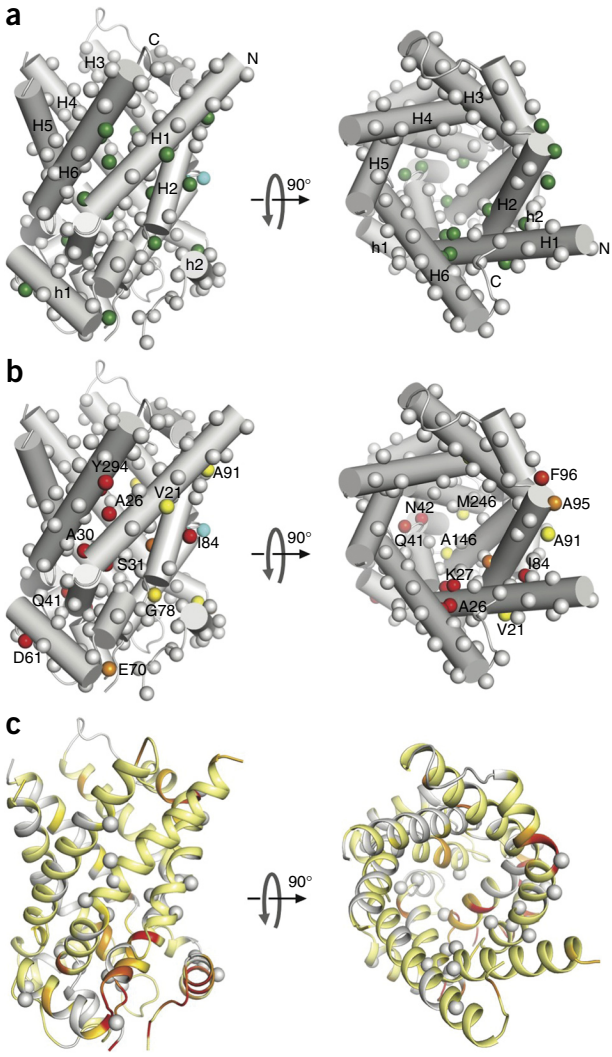

Figure 3 The intrinsic chemical-exchange map of yAAC3. (**a**) Cylinder representation of yAAC3 (PDB 4C9Q[28]) showing backbone-amide ^{15}N nuclei of free yAAC3 with substantial chemical exchange (green spheres). These residues all show $k_{ex} \approx 870 \pm 200\ s^{-1}$. Gray spheres, residues with flat relaxation dispersion curves; cyan sphere, severely exchange-broadened residues. (**b**) Representation as in **a**, showing residue-specific chemical-shift differences ($\Delta\omega$) between the ground and excited states. The spheres are colored according to $\Delta\omega$ value, in a linear gradient from yellow (0.5 p.p.m.) to red (4 p.p.m.). (**c**) Residue-specific chemical-shift changes ($\Delta\Omega$) induced by the addition of 10 mM ADP, mapped to the yAAC3 structure in the same orientation as in **a** and **b**. The $\Delta\Omega$ are shown with a linear color scale from 0.01 p.p.m. (yellow) to 0.03 p.p.m. (red). Residues with strong relaxation dispersion are indicated as gray spheres to illustrate the difference between chemical exchange– and ADP-induced chemical-shift changes.

DISCUSSION

Our relaxation dispersion data show that yAAC3, both free and in the presence of substrate, is predominantly in the c state, which is the low-energy state. The high-energy state accounts for only about 2% of the population at equilibrium. The c state being the ground state is consistent with previous findings that AAC in isolated mitochondria adopts the c-state conformation[23]. We believe that the excited state and the m state are likely to have similar conformations because the large $\Delta\omega$ values are associated with residues of the proline kink (**Figs. 1a** and **3b**), and conformational rearrangements of the proline kinks are required for switching from the c state to the m state[23,24]. Furthermore, residues involved in closing the matrix side of the AAC cavity, namely Gln41, Ala146 and Met246, showed large conformational exchange, which is most probably due to the opening of the matrix side during transitioning from the c state to the m state[23,24]. AAC, with its striking asymmetry in state distribution, is in contrast with many other solute transporters that have more-equal populations of the alternating-access states such as LacY[10], LeuT[7] and EmrE[13]. We acknowledge that the AP helices are positively charged, and thus the presence of membrane potential *in vivo* might affect the population distribution.

The $\Delta\omega$ mapping (**Fig. 3b**) indicates that the switch from the c state to the excited state involves structural rearrangement in the kink regions and the matrix-side region of the odd-numbered helices as well as the N-terminal half of H2. The asymmetric pattern of exchange appears to be an intrinsic property of yAAC3 because neither substrate nor inhibitor significantly altered the $\Delta\omega$ distribution. Ligand binding modulates only the rate of exchange between the two states. We emphasize that the modulation of relaxation dispersion by the ligands is not a consequence of chemical-shift perturbation induced by ligand binding because the chemical-shift changes induced by ADP binding were on average ~50-fold smaller than the $\Delta\omega$ values of conformational exchange and were associated with a different set of residues from those showing relaxation dispersion (**Fig. 3c**). The observation that CATR binding slowed conformational exchange by more than five-fold is consistent with successful crystallization of AAC having been achieved thus far only in the presence of CATR[27,28], which may facilitate crystal formation by making the AAC less dynamic. In contrast to CATR, ADP increases the exchange rate from 800 to 1,800 s^{-1}, and the fast rate is compatible with AAC's being a fast transporter (rate ~400 s^{-1} observed in liposome assays[25]). Earlier studies using NMR and FRET on EmrE[27,28] and LeuT[27,28] have shown that substrates are capable of modulating the transition rate between inward-open and inward-closed states without changing the population distribution between the two states[27,28].

A conceptual model of the ligand-modulated dynamics of AAC can be proposed on the basis of our NMR measurements and previous functional data. The rate of chemical exchange as derived from relaxation dispersion data is determined by the energy barrier separating the two alternating-access states required for transport (**Fig. 4a**). Binding of substrate lowers the activation energy either by destabilizing the c state or by stabilizing the transition state, thus resulting in an increase by more than two-fold in the exchange rate. Conversely, CATR binding raises the activation energy, and this can be explained by two possible mechanisms. First, CATR binding stabilizes the c state and would lower the energy of the c state and thus alter the population distribution between the c state and the excited state. However, because a five-fold decrease in rate results in an ~1.5% decrease in the excited population, which is the same as the uncertainty in p_e (**Table 1**), we cannot conclude whether or not CATR binding lowers the energy of the c state. Another possible mechanism is that CATR binding does not necessarily lower the energy of the c state but instead functions as a molecular wedge that attenuates the transition from the c state to the excited state. In this case, the energy barrier between the two states would be raised without changing the relative populations of the states. This is a more likely scenario because CATR binds mainly to the side of the AAC cavity that shows strong exchange.

Transporters have been optimized to selectively transport substrates. It is conceivable that they adopt structures for which the interconversion

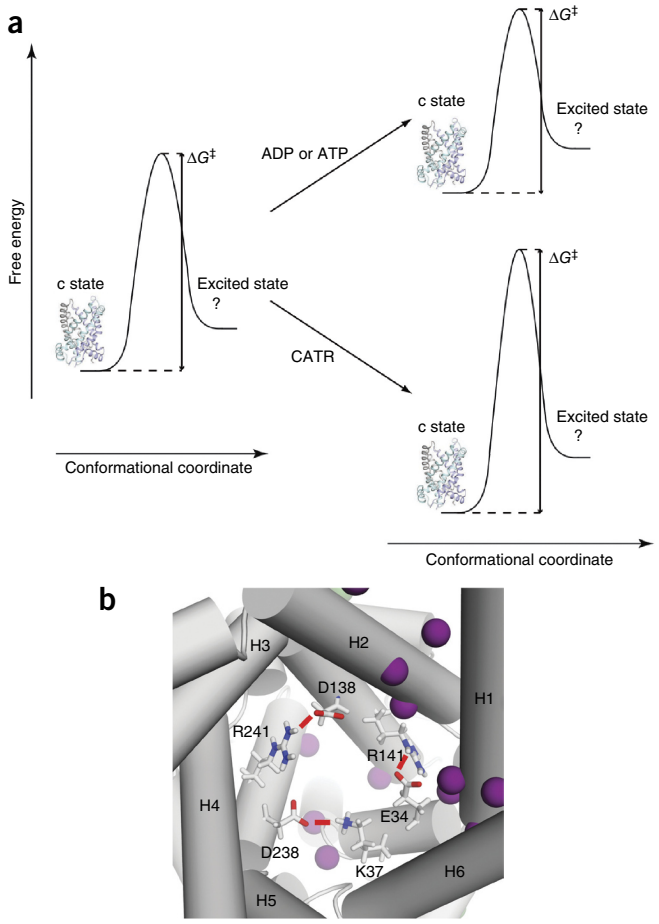

Figure 4 A model for explaining ligand-modulated conformational exchange of AAC. (**a**) Energy diagrams of AAC in the absence and presence of ligands. The low-energy state of the free AAC adopts the c-state conformation, which is represented by the crystal structure. The c state transiently switches to a high-energy excited state, for which the structure is unknown. The binding of the inhibitor CATR raises the activation energy of the conformational switch, whereas the binding of the substrate ADP lowers the activation energy. (**b**) A deep view into the yAAC3 cavity, showing three acidic and three basic residues forming a network of interhelical salt bridges (red lines) that 'locks' the proline-kink segments in a conformation that closes the matrix side of the cavity. ADP pyrophosphate is expected to transiently form salt bridges with the basic residues, thus disrupting the interhelical salt bridges facilitating the conformational switch to the excited state. This mechanism is consistent with the large chemical exchange observed for this region of the yAAC3 cavity in the presence of ADP (purple spheres; additional structures in **Supplementary Fig. 4**).

between two alternating-access states can be selectively facilitated by the designated substrate. For yAAC3, the ADP-facilitated switch from the c state to the excited state can be explained by the structure of the c state and the proposed ADP-binding site[5,36]. In the c-state crystal structure, the closed matrix side of the cavity is stabilized by a network of interhelical salt bridges that hold the odd-numbered TM helices together (**Fig. 4b**). These salt bridges are formed between Glu34 and Arg141, Lys37 and Asp238, and Asp138 and Arg241 (refs. 5,27,28). It has been predicted, on the basis of an MD simulation and functional data, that upon binding to bovine AAC, the phosphate groups of ADP form multiple salt bridges with the three basic residues and that the adenine ring interacts with a hydrophobic pocket formed by Gly188, Ile189 and Tyr192 of H4 (refs. 5,36). The majority of interactions of ADP with AAC are located in domains I and II, thus potentially explaining the asymmetry of conformational exchange detected by the relaxation dispersion experiments. Furthermore, the MD simulation suggests that ADP directly interacts with Arg141 and Lys37 and consequently disrupts the interhelical salt bridges, thus facilitating opening of the matrix side[5].

METHODS

Methods and any associated references are available in the online version of the paper.

Accession codes. NMR data have been deposited in the Biological Magnetic Resonance Data Bank under accession code 26589.

Note: Any Supplementary Information and Source Data files are available in the online version of the paper.

ACKNOWLEDGMENTS

We thank R. Sounier, M. Berardi and K. Oxenoid for insightful discussion and Z. Liu for collecting CPMG data on the Agilent 800 MHz spectrometer at the National Center for Protein Science at Shanghai, China. S.B. is supported as a recipient of an Erwin Schrödinger postdoctoral fellowship of the Austrian Science Fund (FWF, J3251). This work was supported by US National Institutes of Health (NIH) grant GM094608 (to J.J.C.). The main NMR facility used for this study was supported by NIH grant P41 EB-002026.

AUTHOR CONTRIBUTIONS

S.B., Q.Y. and J.J.C. conceived the study; Q.Y., S.B. and C.R. prepared samples and performed ligand binding assays; S.B. collected and analyzed NMR data; S.B., Q.Y. and J.J.C. wrote the paper.

COMPETING FINANCIAL INTERESTS

The authors declare no competing financial interests.

1. Forrest, L.R., Kramer, R. & Ziegler, C. The structural basis of secondary active transport mechanisms. *Biochim. Biophys. Acta* **1807**, 167–188 (2011).
2. Shi, Y. Common folds and transport mechanisms of secondary active transporters. *Annu. Rev. Biophys.* **42**, 51–72 (2013).
3. Khalili-Araghi, F. *et al.* Molecular dynamics simulations of membrane channels and transporters. *Curr. Opin. Struct. Biol.* **19**, 128–137 (2009).
4. Wisedchaisri, G., Park, M.S., Iadanza, M.G., Zheng, H. & Gonen, T. Proton-coupled sugar transport in the prototypical major facilitator superfamily protein XylE. *Nat. Commun.* **5**, 4521 (2014).
5. Wang, Y. & Tajkhorshid, E. Electrostatic funneling of substrate in mitochondrial inner membrane carriers. *Proc. Natl. Acad. Sci. USA* **105**, 9598–9603 (2008).
6. Akyuz, N., Altman, R.B., Blanchard, S.C. & Boudker, O. Transport dynamics in a glutamate transporter homologue. *Nature* **502**, 114–118 (2013).
7. Erkens, G.B., Hanelt, I., Goudsmits, J.M., Slotboom, D.J. & van Oijen, A.M. Unsynchronised subunit motion in single trimeric sodium-coupled aspartate transporters. *Nature* **502**, 119–123 (2013).
8. Zhao, Y. *et al.* Single-molecule dynamics of gating in a neurotransmitter transporter homologue. *Nature* **465**, 188–193 (2010).
9. Zhao, Y. *et al.* Substrate-modulated gating dynamics in a Na^+-coupled neurotransmitter transporter homologue. *Nature* **474**, 109–113 (2011).
10. Majumdar, D.S. *et al.* Single-molecule FRET reveals sugar-induced conformational dynamics in LacY. *Proc. Natl. Acad. Sci. USA* **104**, 12640–12645 (2007).
11. Hwang, P.M., Bishop, R.E. & Kay, L.E. The integral membrane enzyme PagP alternates between two dynamically distinct states. *Proc. Natl. Acad. Sci. USA* **101**, 9618–9623 (2004).
12. Liu, J.J., Horst, R., Katritch, V., Stevens, R.C. & Wuthrich, K. Biased signaling pathways in beta2-adrenergic receptor characterized by 19F-NMR. *Science* **335**, 1106–1110 (2012).
13. Morrison, E.A. *et al.* Antiparallel EmrE exports drugs by exchanging between asymmetric structures. *Nature* **481**, 45–50 (2011).
14. Nygaard, R. *et al.* The dynamic process of beta(2)-adrenergic receptor activation. *Cell* **152**, 532–542 (2013).
15. Oxenoid, K. & Chou, J.J. The present and future of solution NMR in investigating the structure and dynamics of channels and transporters. *Curr. Opin. Struct. Biol.* **23**, 547–554 (2013).
16. Morrison, E.A. & Henzler-Wildman, K.A. Transported substrate determines exchange rate in the multidrug resistance transporter EmrE. *J. Biol. Chem.* **289**, 6825–6836 (2014).

17. Imai, S. *et al.* Functional equilibrium of the KcsA structure revealed by NMR. *J. Biol. Chem.* **287**, 39634–39641 (2012).
18. Vallurupalli, P., Bouvignies, G. & Kay, L.E. Studying "invisible" excited protein states in slow exchange with a major state conformation. *J. Am. Chem. Soc.* **134**, 8148–8161 (2012).
19. Palmer, A.G. III, Kroenke, C.D. & Loria, J.P. Nuclear magnetic resonance methods for quantifying microsecond-to-millisecond motions in biological macromolecules. *Methods Enzymol.* **339**, 204–238 (2001).
20. Mittermaier, A. & Kay, L.E. New tools provide new insights in NMR studies of protein dynamics. *Science* **312**, 224–228 (2006).
21. Neudecker, P. *et al.* Structure of an intermediate state in protein folding and aggregation. *Science* **336**, 362–366 (2012).
22. Whittier, S.K., Hengge, A.C. & Loria, J.P. Conformational motions regulate phosphoryl transfer in related protein tyrosine phosphatases. *Science* **341**, 899–903 (2013).
23. Klingenberg, M. The ADP and ATP transport in mitochondria and its carrier. *Biochim. Biophys. Acta* **1778**, 1978–2021 (2008).
24. Kunji, E.R. & Robinson, A.J. Coupling of proton and substrate translocation in the transport cycle of mitochondrial carriers. *Curr. Opin. Struct. Biol.* **20**, 440–447 (2010).
25. Gropp, T. *et al.* Kinetics of electrogenic transport by the ADP/ATP carrier. *Biophys. J.* **77**, 714–726 (1999).
26. Monné, M. & Palmieri, F. Antiporters of the mitochondrial carrier family. *Curr. Top. Membr.* **73**, 289–320 (2014).
27. Pebay-Peyroula, E. *et al.* Structure of mitochondrial ADP/ATP carrier in complex with carboxyatractyloside. *Nature* **426**, 39–44 (2003).
28. Ruprecht, J.J. *et al.* Structures of yeast mitochondrial ADP/ATP carriers support a domain-based alternating-access transport mechanism. *Proc. Natl. Acad. Sci. USA* **111**, E426–E434 (2014).
29. Babot, M., Blancard, C., Zeman, I., Lauquin, G.J. & Trezeguet, V. Mitochondrial ADP/ATP carrier: preventing conformational changes by point mutations inactivates nucleotide transport activity. *Biochemistry* **51**, 7348–7356 (2012).
30. Riccio, P., Aquila, H. & Klingenberg, M. Purification of the carboxy-atractylate binding protein from mitochondria. *FEBS Lett.* **56**, 133–138 (1975).
31. Bamber, L., Harding, M., Butler, P.J. & Kunji, E.R. Yeast mitochondrial ADP/ATP carriers are monomeric in detergents. *Proc. Natl. Acad. Sci. USA* **103**, 16224–16229 (2006).
32. Loria, J.P., Rance, M. & Palmer, A.G. III. A TROSY CPMG sequence for characterizing chemical exchange in large proteins. *J. Biomol. NMR* **15**, 151–155 (1999).
33. Korzhnev, D.M., Neudecker, P., Mittermaier, A., Orekhov, V.Y. & Kay, L.E. Multiple-site exchange in proteins studied with a suite of six NMR relaxation dispersion experiments: an application to the folding of a Fyn SH3 domain mutant. *J. Am. Chem. Soc.* **127**, 15602–15611 (2005).
34. Tollinger, M., Skrynnikov, N.R., Mulder, F.A., Forman-Kay, J.D. & Kay, L.E. Slow dynamics in folded and unfolded states of an SH3 domain. *J. Am. Chem. Soc.* **123**, 11341–11352 (2001).
35. Korzhnev, D.M. *et al.* Low-populated folding intermediates of Fyn SH3 characterized by relaxation dispersion NMR. *Nature* **430**, 586–590 (2004).
36. Robinson, A.J. & Kunji, E.R. Mitochondrial carriers in the cytoplasmic state have a common substrate binding site. *Proc. Natl. Acad. Sci. USA* **103**, 2617–2622 (2006).

ONLINE METHODS

Sample preparation. A gene encoding residues 1–307 of the yeast ADP/ATP carrier 3 (yAAC3) with an N-terminal His_6 tag was synthesized by GenScript and was subsequently cloned into the pET21a expression vector. The plasmid containing the yAAC3 insertion was transformed into the *E. coli* BL21(DE3) (New England BioLabs) expression strain. The cells were grown at 37 °C in M9 minimal medium to an OD of ~0.8. After induction with 0.5 mM IPTG, the protein was expressed for 4 h at 37 °C. yAAC3 was expressed in inclusion bodies and refolded according to a previously established protocol to generate folded protein for functional assays[37]. The cells were lysed in buffer containing 20 mM HEPES, pH 7.4, 150 mM NaCl, 30 mM lysozyme and 1 mM β-mercaptoethanol (BME). After centrifugation at 20,000*g* for 30 min, the pellet containing the inclusion body was collected and solubilized with buffer containing 1.67% (w/v) *N*-lauroylsarcosine (sarkosyl), 20 mM HEPES, pH 7.4, 150 mM NaCl, 1 mM BME and 0.05% polyethylene glycol 4000 (PEG). After solubilization at 4 °C for 16 h, the solution was centrifuged at 20,000*g* for 30 min to remove the insoluble debris. The supernatant containing the solubilized yAAC3 was rapidly diluted three-fold with buffer containing 6 mM dodecylphosphocholine (DPC), 20 mM HEPES, pH 7.4, 150 mM NaCl and 200 mM imidazole and was then passed through Ni-NTA resin (Thermo Scientific) preequilibrated with dilution buffer. The protein was eluted in buffer containing 3 mM DPC, 20 mM HEPES, pH 7.4, 150 mM NaCl and 200 mM imidazole. To remove the misfolded protein, the yAAC3 eluate was dialyzed against buffer containing 20 mM HEPES, pH 7.4, and 30 mM NaCl for 4 h and purified with a Hi-trap Q FF column (GE Life Sciences). To further fractionate the active form, the yAAC3 purified from the Q column was loaded onto resins cross-linked with ATP (Jena Bioscience). After extensive washing with buffer containing 20 mM HEPES, pH 7.4, 3 mM DPC and 50 mM NaCl, yAAC3 was eluted with 20 mM HEPES, pH 7.4, 3 mM DPC and 500 mM NaCl and was finally passed through a Superdex 200 size-exclusion column (GE Life Sciences) in FPLC buffer containing 30 mM MES, pH 6.0, 20 mM NaCl, 5 mM BME and 3 mM DPC. The homogenous yAAC3 fractions were pooled and concentrated to produce the final NMR sample containing 0.8 mM yAAC3, 120 mM DPC, 5 mM BME, 30 mM MES, pH 6.0, and 20 mM NaCl.

ITC experiments. The calorimetric titrations were carried out at 30 °C on a MicroCal ITC200 instrument. A solution of 50 μM yAAC3 in buffer containing 30 mM MES, pH 6.0, and 20 mM NaCl with 3 mM DPC was loaded into the sample cell. Carboxyatractyloside (CATR) was dissolved in the same buffer to 1 mM concentration and loaded into the injection syringe. Titration curves were generated by 18 successive injections of 2 μL CATR, spaced at 160-s intervals. The ITC experiments were performed in triplicate, and the data were analyzed with ORIGIN 7. The K_d and the stoichiometry (N) were calculated by fitting the thermograms to one set of binding sites.

NMR resonance assignment. Sequence-specific assignment of backbone $^1H^N$, ^{15}N, $^{13}C\alpha$, $^{13}C\beta$ and $^{13}C'$ resonances was first carried out for the apo-AAC. The triple-resonance experiments used for this purpose include TROSY-based HNCA, HN(CO)CA, HNCACB, HN(CO)CACB, HN(CA)CO and HNCO[38,39]. Additionally, the assignments were validated with a 3D (H^N, H^N)-HSQC-NOESY-TROSY spectrum with ^{15}N, ^{15}N and $^1H^N$ evolution in the t_1, t_2 and t_3 dimensions, respectively, recorded with an NOE mixing time of 250 ms. These experiments were performed with an 0.8 mM $^{15}N/^{13}C/^2H$-labeled apo-AAC sample at 30 °C on a 600-MHz Bruker spectrometer equipped with a cryogenic TXI probe. Resonance assignments were obtained for ~80% of all backbone and $^{13}C^\beta$ resonances. Resonance assignment of the ADP- or CATR-bound state was achieved by tracing the assigned resonances of the apo-AAC when the AAC sample was titrated with increasing amounts of ADP or CATR. The NMR experiments used for the titration are 2D ^1H-^{15}N TROSY-HSQC and 3D TROSY-HNCO recorded under the same conditions. Data were processed with NMRPipe[40] and analyzed with CcpNmr[41].

NMR relaxation dispersion measurements. Backbone ^{15}N single-quantum CPMG relaxation dispersion experiments were performed on a 600-MHz, a 700-MHz, and an 800-MHz Agilent DD2 spectrometer equipped with a third-generation cryogenic probe. The CPMG dispersion experiment measures the modulation of the transverse relaxation rate ($R_2(1/\tau_{cp})$) as a function of the delay (τ_{cp}) between 180° RF pulses. As shown in the data analysis, the R_2 versus τ_{cp} data can be fitted to determine equilibrium populations (p_a, p_b), kinetics ($k_{ex} = k_1 + k_{-1}$) and chemical-shift differences ($\Delta\omega$) between the two interconverting conformations.

Residue-specific R_2 dispersion was measured with the 2D ^{15}N TROSY-CPMG[42] and the 3D TROSY-CPMG-HNCO (**Supplementary Fig. 3**) experiments. Because 35% of the AAC resonances overlapped in the 2D ^1H-^{15}N TROSY-HSQC spectrum, it was essential to record the 3D TROSY-CPMG-HNCO spectra, which provided the large majority of the relaxation dispersion measurements. The CPMG experiments use a 20-ms constant-time ^{15}N relaxation delay with τ_{cp} spacing of 236.778 μs, 271.3 μs, 314.143 μs, 375.667 μs, 459.0 μs, 584.0 μs, 792.333 μs, 1,209 μs and 2,459 μs, which correspond to CPMG-based RF field strengths, ν_{CPMG}, ranging from 100 to 900 Hz (ref. 43). The spectra with different τ_{cp} values were recorded in an interleaved fashion, and duplicate data sets were recorded at two τ_{cp} values for error analysis. All spectra were recorded at 30 °C with 0.8 mM $^{15}N/^{13}C/^2H$-labeled free yAAC3 and the same sample in the presence of 10 mM ADP or 3 mM CATR. For the 2D ^{15}N TROSY-CPMG, 128 data points were recorded in the indirect dimension with 24 scans per point for free AAC and 64 scans for the substrate- and inhibitor-bound states. For the 3D TROSY-CPMG-HNCO experiment, 60 and 25 data points were recorded for the ^{15}N and ^{13}C indirect dimension, respectively, with eight scans per point.

NMR relaxation dispersion data analysis. Conformational exchanges of free AAC, AAC in the presence ADP and AAC bound to CATR are in the intermediate-to-slow exchange regime (150–1,800 s^{-1}). To avoid systematic errors in fitting different time regimes, all dispersion curves were fit to an exact numerical solution of the Bloch equation with a model of two-site exchange to obtain the calculated relaxation rates $R_{2,eff}^{calc}$ (refs. 43,44). The parameters of the two-site exchange model, rate of conformational exchange, k_{ex}, the populations of the two involved states, (p_a and p_b) and the ^{15}N chemical-shift difference between the two states, Δω, were obtained by performing least-square fits to minimize

$$\chi^2 = \sum \frac{\left(R_{2,eff}^{calc} - R_{2,eff}^{\exp}\right)}{\left(\Delta R_{2,eff}^{\exp}\right)}$$

where $R_{2,eff}^{\exp}$ and $R_{2,eff}^{calc}$ are the experimental and calculated relaxation rates, respectively, and the summation is over all residues included in the fit. The uncertainties in relaxation rates are given by $\Delta R_{2,eff}^{\exp}$ and were calculated from repeat experiments as described previously[44].

First, relaxation dispersion profiles with R_2 exchange contributions >4 s^{-1} were fit with individual exchange parameters to a two-site exchange model to yield residue-specific values for the rate of exchange, k_{ex}, the chemical-shift difference between the two states, $\Delta\omega$, and the populations of the states, p_i. In a second step, residues with similar k_{ex} and p_i values were fit in global fits assuming uniform rate constants and populations but site-specific values for $\Delta\omega$, because the use of a global fit and the use of multiple magnetic fields led to a higher certainty in the obtained parameters[45,46]. In a third step, residues with R_2-exchange contributions between 2 s^{-1} and 4 s^{-1} were fit individually, with k_{ex} and p_i constrained to the values obtained from the global fit to determine their $\Delta\omega$.

37. Heimpel, S., Basset, G., Odoy, S. & Klingenberg, M. Expression of the mitochondrial ADP/ATP carrier in *Escherichia coli*: renaturation, reconstitution, and the effect of mutations on 10 positive residues. *J. Biol. Chem.* **276**, 11499–11506 (2001).
38. Kay, L.E., Torchia, D.A. & Bax, A. Backbone dynamics of proteins as studied by ^{15}N inverse detected heteronuclear NMR spectroscopy: application to staphylococcal nuclease. *Biochemistry* **28**, 8972–8979 (1989).
39. Pervushin, K., Riek, R., Wider, G. & Wuthrich, K. Attenuated T2 relaxation by mutual cancellation of dipole-dipole coupling and chemical shift anisotropy indicates an avenue to NMR structures of very large biological macromolecules in solution. *Proc. Natl. Acad. Sci. USA* **94**, 12366–12371 (1997).

40. Delaglio, F. *et al.* NMRPipe: a multidimensional spectral processing system based on UNIX pipes. *J. Biomol. NMR* **6**, 277–293 (1995).
41. Vranken, W.F. *et al.* The CCPN data model for NMR spectroscopy: development of a software pipeline. *Proteins* **59**, 687–696 (2005).
42. Loria, J.P., Rance, M. & Palmer, A.G. III. A TROSY CPMG sequence for characterizing chemical exchange in large proteins. *J. Biomol. NMR* **15**, 151–155 (1999).
43. Tollinger, M., Skrynnikov, N.R., Mulder, F.A., Forman-Kay, J.D. & Kay, L.E. Slow dynamics in folded and unfolded states of an SH3 domain. *J. Am. Chem. Soc.* **123**, 11341–11352 (2001).
44. Korzhnev, D.M., Neudecker, P., Mittermaier, A., Orekhov, V.Y. & Kay, L.E. Multiple-site exchange in proteins studied with a suite of six NMR relaxation dispersion experiments: an application to the folding of a Fyn SH3 domain mutant. *J. Am. Chem. Soc.* **127**, 15602–15611 (2005).
45. Ishima, R. & Torchia, D.A. Error estimation and global fitting in transverse-relaxation dispersion experiments to determine chemical-exchange parameters. *J. Biomol. NMR* **32**, 41–54 (2005).
46. Kovrigin, E.L., Kempf, J.G., Grey, M.J. & Loria, J.P. Faithful estimation of dynamics parameters from CPMG relaxation dispersion measurements. *J. Magn. Reson.* **180**, 93–104 (2006).

doi:10.1038/nsmb.3059